ADVANCED FUNCTIONAL MATERIALS
www.afm-journal.de

Unleashing 2D MXene's Plasmonic Effect for Advanced Photonic Device Applications

Moonjeong Jang, Seoung Hyun Kim, Shinho Kim, Kwanbyung Chae, Sodam Choi, Hwi Heon Ha, Jungchul Song, Min Jun Bak, Su-Ho Cho, Eunji Kim, Wooseok Song, Hee Han, Min Seok Jang, Chi Won Ahn,* and Yonghee Lee**

MXenes, the largest family of 2D transition metal carbides/nitrides, have emerged as promising materials for various applications due to their exceptionally fascinating properties. In this study, the potential of MXenes is investigated in plasmonic applications, particularly focusing on surface-enhanced Raman scattering (SERS) and broadband photodetection. The study explored a broader range of light-matter interactions based on edge plasmons that emerge at sub-monolayer coverage of MXene, while existing studies have primarily focused on thicknesses exceeding tens of nanometers. Additionally, by incorporating MXenes onto 3D trench nanostructures, To maximize their plasmonic properties is aimed by enhancing the manifestation of edge plasmons, leading to intensified light amplification. The fabricated opto-electronic devices exhibit remarkable sensitivity in SERS detection, achieving a detection limit as low as ≈0.1 nM for the target dye molecule, significantly surpassing typical thresholds for non-metal-based detection. Additionally, the enhancement factor exceeds that of commercially available Au-based SERS substrates. Furthermore, MXene-based photodetectors demonstrate competitive photoresponsivity and response time, particularly toward the near-infrared (NIR) wavelength bands, which are challenging to achieve with MXene-based photodetectors. Through a comprehensive analysis, including electric field calculations, the mechanisms driving the observed enhancements are unveiled, primarily attributing them to edge plasmons.

1. Introduction

With the advent of nanofabrication techniques, high-intensity converging light ability with noble metallic surfaces such as silver or gold nanoparticles offers a path toward the detection system deployment of optoplasmonic sensors. These techniques help overcome the issue of limited sensitivity for sensor signal amplification. Surface-enhanced Raman scattering (SERS) is a method commonly adopted for sensing in which inelastic light scattering by molecules is substantially boosted when the corrugated metal surfaces are used to generate surface plasmons for the adsorbed molecules.[1–6] These metallic nanomaterial resonant structures are provided by the large optical field enhancement achieved through appropriately sized intergaps and morphologies, rendering them effective as SERS-active substrates. In particular, to benefit from both electromagnetic mechanism and chemical mechanism enhancements in the visible and infrared SERS applications, enhancing the low intensity of Raman scattering in 2D plasmonic materials should be further explored.[7–10]

M. Jang, S. H. Kim, K. Chae, S. Choi, H. H. Ha, J. Song, M. J. Bak, S.-H. Cho, E. Kim, H. Han, C. W. Ahn, Y. Lee
National Nano Fab Center (NNFC)
Daejeon 34141, Republic of Korea
E-mail: cwahn@nnfc.re.kr; yhlee@nnfc.re.kr

S. Kim, M. S. Jang
School of Electrical Engineering
Korea Advanced Institute of Science and Technology (KAIST)
291 Daehak-ro, Yuseong-gu, Daejeon 34141, Republic of Korea
E-mail: jang.minseok@kaist.ac.kr

W. Song
Thin Film Materials Research Center
Korea Research Institute of Chemical Technology (KRICT)
Daejeon 34114, Republic of Korea

W. Song
School of Electronic and Electrical Engineering
Sungkyunkwan University
Suwon 16149, Republic of Korea

The ORCID identification number(s) for the author(s) of this article can be found under https://doi.org/10.1002/adfm.202405341

DOI: 10.1002/adfm.202405341

In this context, 2D MXenes, a new family of transition metal carbides/nitrides, have received significant scientific attention based on their outstanding inherent properties associated with longer electronic mean free paths to prolong electron-electron scattering relaxation time and relatively slow recombination dynamics of surface plasmon.[11–19] However, 2D MXene possesses relatively lower electronic density and more complex physics of the electromagnetic mechanism compared with that of classical plasmonic metal nanospheres.[20–22] For these non-spherical structured metallic materials, it is advantageous to involve the plasmonic hotspot gap distance and more geometrical details related to field strengths for light converging arising from nanostructured metals. Therefore, the specific methodology of arrangement in subnano-sized hotspots is crucial in enabling the design of active substrates tailored for desired optoplasmonic applications.[23,24]

In this work, we aim to develop the photonic and opto-electronic devices comprising single-material-based surface plasmon-driven SERS and broadband photodetection for identifying both electromagnetic mechanisms and chemical mechanisms in 2D Ti_3C_2 MXene. In previous research, MXene's SERS applications were predominantly explored primarily at thicknesses exceeding tens of nanometers, with a particular emphasis solely on the chemical mechanism.[18,25] In contrast, our study delves into a realm beyond, investigating the significantly amplified scale of light-matter interaction occurring at sub-monolayer coverage of MXene, facilitated by the computation of MXene's edge plasmons, deeply related to the electromagnetic mechanism. Furthermore, we augmented this optical enhancement by incorporating 3D trench nanostructures. The nanostructured MXene deposited onto dielectric trenches that act as the SERS-active light signal amplifier was realized by the cooperation between enhanced charge transport and surface plasmon-induced hot carrier injection. Our developed SERS sensing platform achieved exceptionally high detection sensitivity, with detection limits as low as ≈0.1 nM for the target dye molecule (rhodamine 6G (R6G)). This represents a remarkable advancement in non-metal-based detection limits, enabled by the intensified edge plasmon on the 3D nanostructures. The proposed strategy also offers key advantages in terms of accomplishing Ti_3C_2 MXene-based photodetectors with competitive photoresponsivity and response time, simplicity of device structure, and low power consumption. Especially noteworthy is the exceptional photocurrent observed in partially freestanding MXenes on 3D trench nanostructures within the near-infrared (NIR) wavelength bands, a realm where prior research on MXene-based photodetectors has been limited. These findings provide insightful perspectives into the interaction between MXenes and light, elucidating their potential in various optical domains and paving the way for promising future photonic and opto-electronic applications.

2. Results and Discussion

$Ti_3C_2T_x$ MXene was spin-coated onto both a flat Si/SiO_2 substrate and a 3D Si/SiO_2 trench substrate to investigate their optical behaviors, particularly as SERS substrates, while also exploring its performance in plasmonic light-matter interactions as photodetectors. In the case of the Si/SiO_2 trench used as a substrate, a line & space structure was designed with an interval of 40 nm, and a depth of 50, 80, and 100 nm using an ArF scanner. The interval of 40 nm was chosen as it represents a fine pattern resolution that can be reliably achieved with current nanofabrication techniques. Depths of 50, 80, and 100 nm were selected to systematically study the plasmonic effects at different depths. **Figure 1** illustrates the manufacturing method for the MXene-based 3D nanostructures and their exploration in plasmonic applications. Following fabrication, the substrate underwent a thorough cleaning process involving ethanol, acetone, and isopropyl alcohol, followed by surface treatment using air plasma and 3-Aminopropyltriethoxysilane (APTES) solution to enhance the bonding strength between MXene and the substrates. MXene was uniformly coated at concentrations ranging from 10% to 100% using the spin coating method, as detailed in the experimental sections.

2.1. Fundamental Analysis and Optical Characterization of MXene

The chemical features of the synthesized MXene were analyzed via X-ray photoelectron spectroscopy (XPS). After the formation of MXene etched from the MAX phase, the Ti-C (E_B = 455.2 and 461.0 eV) and C-Ti (E_B = 282.1 eV) bonding states were discernible at the constituent Ti *2p* and C *1s* core level spectra (**Figure 2**a,b). Additionally, Figure 2c exhibits that the Al *2p* core level spectrum provides complete elimination of Al, as evidenced by the absence of an Al-related bonding state for MXene. These XPS results unambiguously reveal that the MXene is a well-etched Ti_3C_2 phase.[26] In Figure 2d, the scanning electron microscopy (SEM) image of MXene, coated with ≈60% coverage, displays a uniformly coated surface with flakes measuring ≈ 1 µm in size. Notably, no discernible formation of TiO_2 particles was identified. Surface analysis using atomic force microscopy (AFM) revealed the size of MXene to be ≈1 µm, with a thickness of ≈ 1.6 nm, indicating a well-etched single-layer MXene.[27] The AFM-based thickness analysis revealed no height difference exceeding 1 nm, confirming the absence of defects in the synthesized MXene phase (Figure 2e,f).

In evaluating the applicability of MXene as SERS substrates, R6G was chosen as the probed dye due to its commercial availability, high stability, and effective detectability on various substrates. The UV-vis absorption spectra of R6G and MXene in a water solution are presented in **Figure 3**. The noticeable absorbance peak around 527 nm is evident, and with a transition from an R6G concentration of 10^{-6}–10^{-5} M, the detectable peak is enhanced without any peak shifting, as shown in Figure 3a. Accordingly, a 532 nm wavelength laser source was chosen due to the position of the R6G absorption peak, enabling high excitation SERS spectra at 532 nm in this study.

As shown by the UV-vis absorption spectra in Figure 3b, a broad absorption band ≈750 nm was assigned to MXene originating from the π-plasmon of carbon.[28,29] After mixing MXene in a water solution with R6G, the presence of a remarkable absorbance peak of R6G was confirmed compared with MXene. In addition, it should be noted that the position of the absorption peak of the dye red-shifted to 544 nm after mixing dye with MXene. In most cases, analysis by UV-vis absorption spectroscopy reveals a bathochromic (to higher wavelengths) shift of

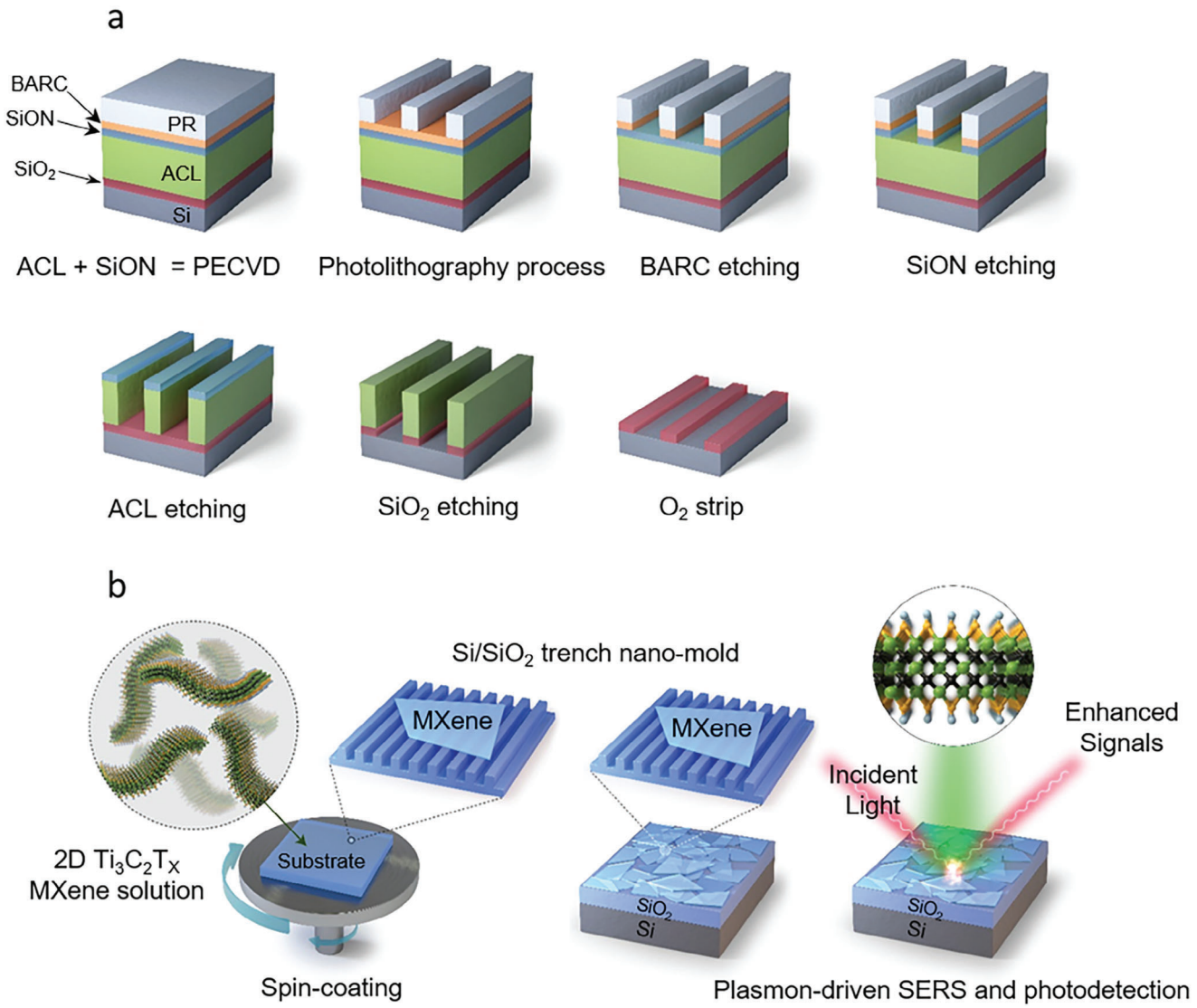

Figure 1. Schematics illustrating a) photolithography and dry etching process for fabricating the 3D Si/SiO_2 trench substrate, including photoresist (PR), bottom anti-reflection coating (BARC), silicon oxynitride (SiON), amorphous carbon layer (ACL), and b) the $Ti_3C_2T_x$ MXene-based plasmon-enhanced light-matter interaction.

the conjugated compounds, which is caused by higher energy transitions. Thus, the extent of the red shift is attributable to the strength of the chemical interaction between the R6G and MXene surface.[30,31]

Since the 2D structures are atomically thin and flat, direct contact and rapid charge transfer between host and guest would be facilitated to produce much dye molecule detection. Notably, the MXene formed on trench patterned structure demonstrates enhanced capturing of target R6G molecules compared to the flat structure, leading to increased electron transfer from MXene to R6G. Thus, the Raman intensity can be enhanced by increasing the dipole moment and polarizability of dye molecules. In addition, in the partially freestanding MXene formed on the trench structure, the effect of charge trapping (electron-hole puddles) occurring at the MXene-substrate interface can be excluded in SERS. This direct charge transfer phenomenon between R6G and MXene was analyzed through UV–vis absorption spectroscopy.

To study the dependence of the SERS performance on the partially freestanding MXene deposition, the phonon modes of the spin-coated MXene on nanopatterned Si/SiO_2 substrates with line-width 40 nm and 50, 80, and 100 nm depths were proceeded by Raman spectroscopy. As presented in Figure 3c, the Raman peaks at 205, 371, 619, and 718 cm^{-1} are the characteristic phonon modes for Ti_3AlC_2 MXene.[32–34] The peaks at 205 and 718 cm^{-1} correspond to the out-of-plane (A_{1g}) modes of O-terminated $Ti_3C_2O_2$. The peaks at 371 cm^{-1} were attributed to the O atoms in-plane (E_g) vibrations, and those at 619 cm^{-1} were mainly caused by the Eg vibrations of the C atoms in the OH-terminated Ti_3C_2. The resulting patterned substrates show that the Raman signal rises as the line pattern depth is increased up to 100 nm, compared with the MXene on the flat substrate. The

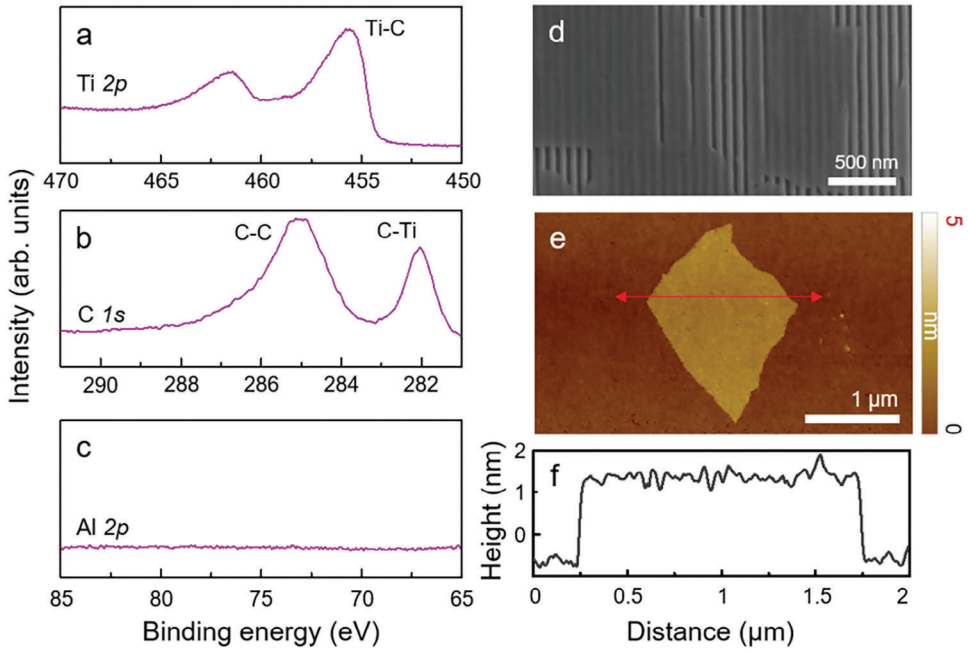

Figure 2. XPS core level spectra of a) Ti *2p*, b) C *1s*, and c) Al *2p* of MXene. d) Top-view SEM image of MXene on the trench substrate. e) AFM image of single layer MXene and f) AFM-derived height information for MXene.

cross-sectional SEM images of MXene on the trench substrate clearly indicate the successful fabrication of partially freestanding MXenes, as shown in Figure S1 (Supporting Information). The observed variation in the depth-dependent Raman signal of MXene originates from enhanced light-matter interaction due to interference between incident and reflected light on the trench surface (Figure S2, Supporting Information). These findings also provide substrate-dependent Raman behavior of 2D MXene, owing to a directional correlation between the trench depth and height of the partially freestanding. Hence, an investigation on the substrate geometry-dependent Raman activity of MXenes is accompanied by the formation of partially freestanding regions, yielding surface plasmon-induced local electromagnetic field enhancements. To confirm the optical lateral behavior of MXene, different thicknesses of MXene were measured using an ellipsometer (Figure 3d). As the MXene stack is thinned to a single layer, the real part of the permittivity near the wavelength of the light source gradually decreases. At an effective thickness of 0.9 nm, the permittivity of MXene changes to a negative value, indicating metallic behavior. This metallic behavior enables significant enhancement of the Raman signal through plasmon polaritons, which have been reported in the near-infrared range for multiple layers of MXene.[35,36] This indicates that a single layer of MXene supports plasmon polaritons even in the visible region, unlike multiple layers of MXene, where plasmon polaritons are excited only in the near-infrared region. Despite having an effective thickness less than that of a single layer (1.6 nm), which implies potential inaccuracies in ellipsometry measurements due to incomplete coverage of MXene on the surface of the SiO_2/Si substrate, the experimentally observed Raman signal enhancement indicates the excitation of a highly confined plasmon on the edge and surface of partially covered single-layer MXene.

2.2. Nanostructure-Enhanced Plasmonics for SERS Applications

Exploration of the impacts of the concentration of R6G and coverage of MXene on Raman enhancement was implemented by Raman spectroscopy. A facile manipulation of the coverage of MXene was accompanied by controlling the concentration of MXene solution combined with the surface treatment of flat Si/SiO_2 using plasma cleaning and APTES.[37] **Figure 4a** displays comparative Raman spectra acquired from 10^{-6} M R6G on the SiO_2 substrate with and without MXene. While the R6G-related Raman modes were not detected on the substrate without MXene, the R6G-related modes could be clearly ascertained on the substrate with MXene, which signals a clear evidence of the SERS effect of MXene. Figure 4b illustrates Raman spectra of R6G with altered concentration (10^{-6}–10^{-4} M) on MXene (80% coverage) flat substrate. The intensity exhibited a linear increase with ascending R6G concentration, confirming the detection of R6G down to a concentration of 10^{-7} M under MXene (coverage 80%) conditions on a flat SiO_2 substrate. Figure 4c shows the SEM images of coverage and thickness according to the aforementioned MXene concentration. A reduction in the MXene aqueous solution concentration resulted in a decrease in both the thickness of MXene and its coverage on the substrate. The thickness and surface characteristics of MXene were analyzed using AFM, as depicted in Figure S3 (Supporting Information). The thickness of the MXene layer was measured at coverages of 50, 60, 90, and 100%. The average values for each concentration were found to be 0.3, 1, 0.5, and 1.2 nm, respectively, while the baseline values were recorded as 0.4, 0.9, 0.8, and 1.7 nm. The thickness of a single layer of MXene was ≈1.6 nm, indicating effective surface coverage with minimal agglomeration. Optical properties exhibited variations corresponding to changes in the thickness and coverage of MXene, as illustrated in the Raman analysis results (Figure 4d–f). As the

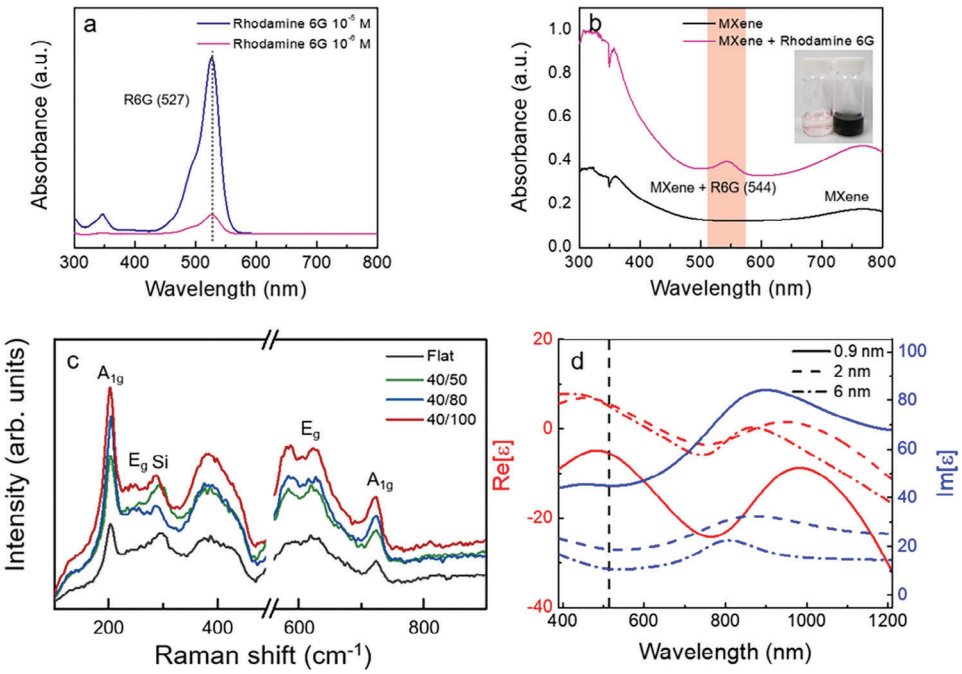

Figure 3. a) UV–vis absorption spectra of R6G in a water solution. b) Comparative analysis of UV–vis absorption spectra between MXene and 10^{-6} M R6G with MXene. c) Comparative Raman spectra of MXene spin-coated onto flat Si/SiO_2 and Si/SiO_2 trench with line widths of 40 nm and depths of 50, 80, and 100 nm. d) Dielectric functions of MXene layers. The left (red) and right (blue) axes represent the real and imaginary parts of permittivity, respectively. The black dashed line indicates the wavelength of the excitation light source.

coverage of MXene coated on the SiO_2 substrate increased, the intensity exhibited an upward trend. However, the intensity subsequently decreased as both coverage and layer increased beyond 60%. As the edge portion of the MXene flake expanded, the Raman intensity increased. In Figure S4 (Supporting Information), the total length of the MXene flake edge exhibited an increase up to a coverage of ≈ 50%, followed by a sharp decrease after reaching 60%. However, beyond a certain coverage, a sharp decrease occurred, notably from above 100% coverage, indicating that each MXene flake can function as an individual structure, and the observed plasmonic enhancement in the MXene-based substrate is strongly correlated with its edge effect. To further investigate the above phenomenon, the edge length was checked according to MXene coverage. These findings align with the observed pattern in Raman intensity by coverage. This shows that the electromagnetic mechanism effect caused by the plasmonic effect occurring at the edge of MXene has a dominant influence on the SERS effect in single-flake MXenes rather than the chemical mechanism caused by the ligand present on the surface of MXene.

A line & space 3D structure (trench substrate) was formed on a Si/SiO_2 substrate using an ArF scanner, and the concentration of MXene was adjusted to achieve varying coverage and thickness. The 3D structure was formed with a line width of 40 nm and depths of 50, 80, and 100 nm. In **Figure** 5a, Raman measurements were conducted to observe changes in Raman intensity corresponding to the depth of the trench substrate. The measurements were performed under consistent MXene coverage conditions, using R6G (10^{-6} M) as an indicator. SEM images of MXene coated on trenches with different thicknesses (40 nm/100 nm) are presented in Figure S5 (Supporting Information). The measured Raman intensity increased proportionally with the depth of the trench mold. Notably, the enhancement factor (EF) on a substrate with a depth of 100 nm was ≈5 times higher than the Raman intensity in a flat structure. When compared to highly sensitive, commercially available 3D Au SERS substrates as a reference, our developed SERS substrates exhibited even higher optical enhancement. The EF value for the sample with the 40 nm/50 nm depth was nearly equivalent to that of the commercially available 3D Au SERS substrates, whereas the EF value for the 40 nm/100 nm depth sample exceeded it by 1.5 times (Figure 5b). To ascertain the limit detection of R6G at the highest EF depth of 100 nm and to validate the linearity of Raman intensity concerning R6G concentration, Raman spectra were examined at R6G concentrations ranging from 10^{-4} to 10^{-10} M (Figure 5c,d). Under the same MXene coverage, it was confirmed that the Raman intensity exhibited linear growth with increasing R6G concentration, and detection was viable even at an R6G concentration as low as 10^{-10} M (Figure 5d). The Raman intensity according to the coverage of MXene coated on the trench substrate is shown in Figure 5e. The Raman shift of MXene coated on the trench mold at varying coverages is illustrated in Figure S6 (Supporting Information). Similar to flat substrates, high EF values were observed when MXene coverage ranged from 40 to 60%, surpassing three times the EF values of flat substrates. The trench substrate played a pivotal role in forming a more robust hot spot at the edge of a single flake of MXene, increasing the local surface area of MXene by enhancing its surface roughness. Moreover, the increasing trench depth introduced additional effects such as reflected waves from the light source, contributing to higher EF values at appropriate depths. The trace

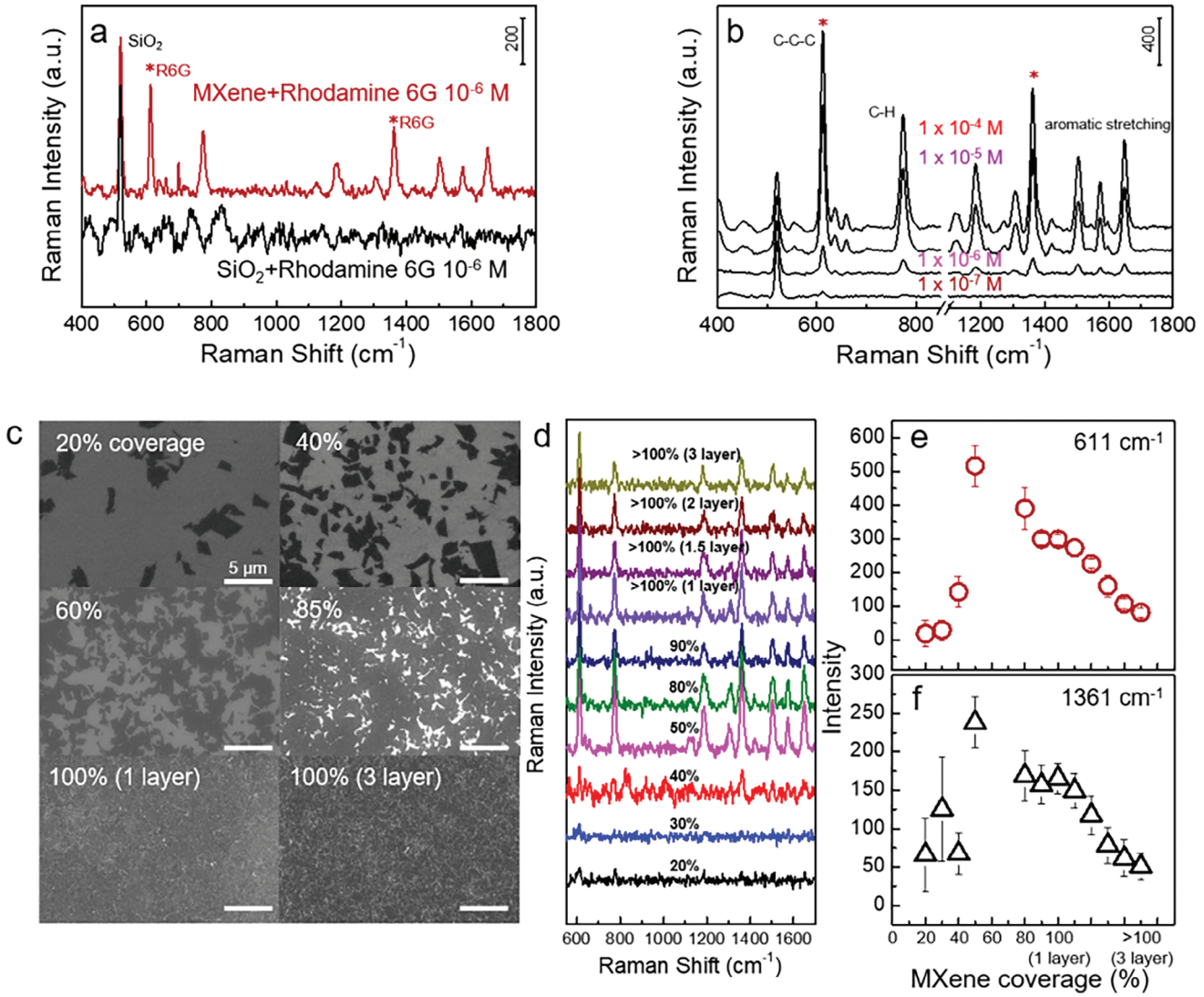

Figure 4. a) Comparative Raman spectra acquired from 10^{-6} M R6G on SiO_2 and MXene flat substrates. b) Raman spectra of R6G with altered concentration (10^{-7}–10^{-4} M) on MXene (80% coverage) flat substrate. c) Representative SEM images of MXene with different surface coverage on Si/SiO_2 substrate. d) Raman spectra of 10^{-6} M R6G on MXene with varied coverage (20∼ >100% (3 layers)). Evolution of Raman intensities of R6G peaks at e) 611 and f) 1361 cm^{-1} as a function of MXene coverage.

detection of methylene blue (MB) was further validated by using the comparative Raman spectra of MB adsorbed on Si/SiO_2 and MXene with flat Si/SiO_2 and Si/SiO_2 trench (100 nm depth) substrates, as displayed in Figure S7 (Supporting Information). On the MXene-coated flat Si/SiO_2 substrate, the Raman modes of MB were detectable, demonstrating the inherent SERS activity of MXene. However, the most significant enhancement was observed on the MXene-coated Si/SiO_2 trench substrate, where the Raman intensity of the MB peaks was markedly higher at ≈ 1395 and 1623 cm^{-1}. This confirms the effectiveness of our 3D trench nanostructures in enhancing the SERS signal for different chemicals, demonstrating the universality and practical applicability of the MXene-based SERS platform. Figure 5f displays the outcomes of a four-week reliability test conducted at 60% MXene coverage. The Raman intensity measured four weeks after the initial application of R6G (10^{-6} M) showed no significant difference, indicating that MXene coated on the Si/SiO_2 trench substrate exhibited a reliability duration of 4 weeks.

2.3. Analysis of Electromagnetic Mechanism in Raman Enhancement

To comprehend the underlying electromagnetic mechanism in the Raman enhancement of MXene, the electric field EF for a single-layer MXene flake on top of various substrate geometries was calculated. To reveal the mechanism of observed Raman signal enhancement as a function of coverage, electric field EF for the surface and edge of the MXene flakes were computed separately. The electric field EF exhibits weak dependence on the lateral dimension of flakes (Figure S8, Supporting Information), indicating that the contribution of plasmonic enhancement to

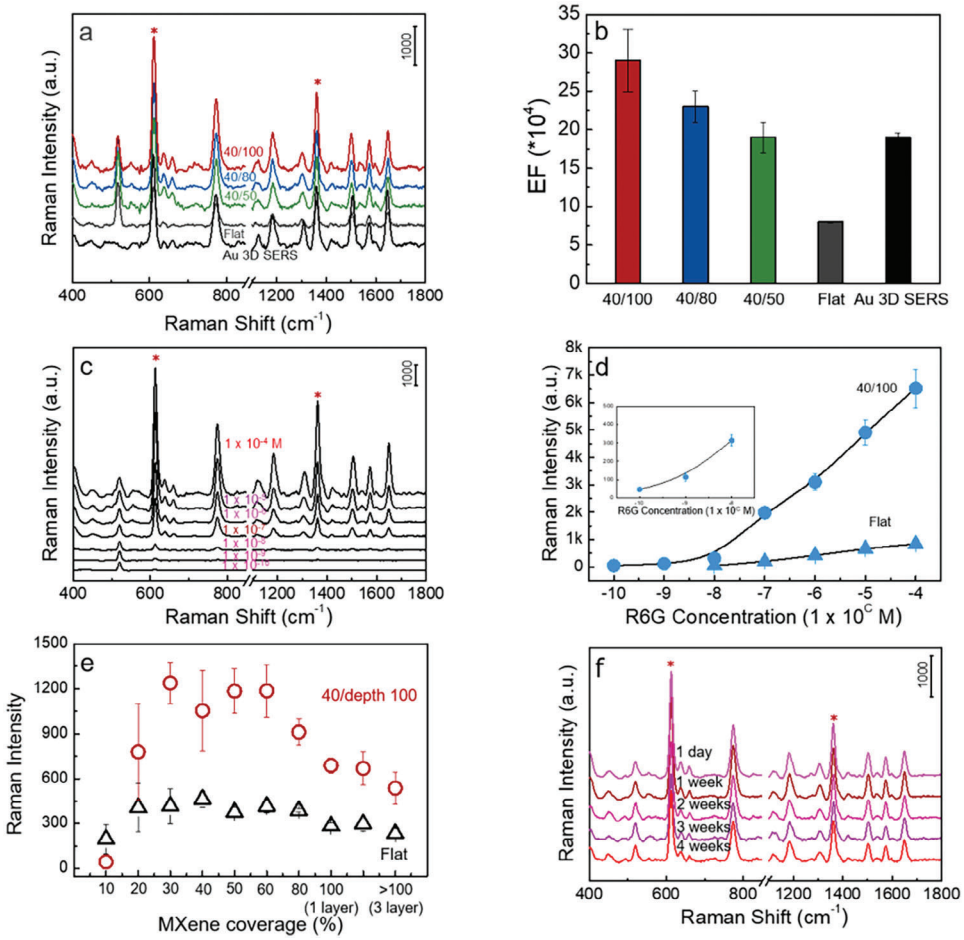

Figure 5. a) Substrate-dependent Raman spectra of 10^{-6} M R6G adsorbed on MXene. b) EF of 10^{-6} M R6G according to substrate type. c) Raman spectra observed at varying concentrations of R6G on Si/SiO_2 trench substrates with a line width of 40 nm and a depth of 100 nm. d) Raman spectra corresponding to different R6G concentrations with flat Si/SiO_2 and Si/SiO_2 trench substrates. e) Comparative analysis of Raman intensity between flat Si/SiO_2 and Si/SiO_2 trench substrates. f) Temporal evolution of the Raman spectra of 10^{-6} M R6G on MXene trench substrate.

electromagnetic mechanism in Raman enhancement could be treated separately. Each EF is derived from the electric field EF weighted by surface area to account for the area-dependent relative strength of each contribution, as shown in **Figure 6**a. To quantify the edge contribution, the effective surface area was defined as the product of the boundary length obtained from SEM images and 1 nm, which is comparable to the lateral size of R6G molecules. This effective surface area is validated by the sparse distribution of adsorbed R6G molecules on the surface and edge of the MXene (Figure S9, Supporting Information). Figure 6b illustrates that the total EF is well matched to the observed Raman signal enhancement, indicating the primary contribution to Raman signal enhancement originates from the strongly confined edge plasmon of MXene flakes.

To better understand the remarkable properties exhibited by the trench structure, we compared the electric field distribution of flat and 40 nm/100 nm substrate structures for transverse magnetic polarized incident light, as shown in Figure 6c. Similar to conventional plasmonic field confinement,[38,39] the electric field is greatly intensified at the edges of the MXene flakes due to charge accumulation (edge plasmons). Compared to the flat substrate, the edge plasmon of MXene on top of the trench substrate provides stronger electric field enhancement. Additionally, periodic permittivity perturbation induced by SiO_2 posts leads to plasmonic hot spots and an increase in the active surface area.[40] The calculation of the EF dependent on trench depth aligns well with the observed Raman signal enhancement, which arises from the interference between incident and reflected light at the interface of SiO_2 and Si layers.[41] Trench depth alters the optical path length of reflected light, resulting in fluctuations in the EF due to alternating electric field strengths at the surface of the MXene, which depends on the degree of constructive interference (Figure 6d).

2.4. Enhanced Photodetection with Nanostructured MXene

To unveil the surface plasmon effects of MXene films on the photoelectrical performance, broadband photodetectors based on MXene films on flat Si/SiO_2 substrates and partially freestanding MXene films on Si/SiO_2 trench were fabricated. To form electrical contacts for two-terminal photodetectors, 3 nm-thick Cu and

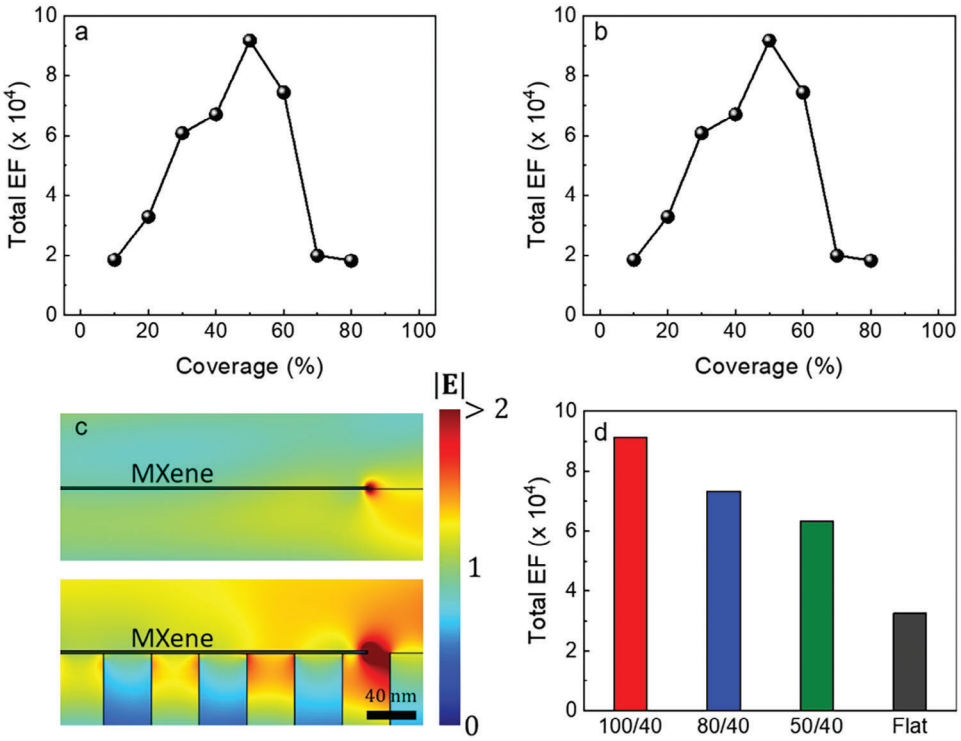

Figure 6. Calculated electric field EF for a) each individual contribution and b) the total contribution. c) Electric field distribution comparison between flat (upper) and trench (lower) structures demonstrating distinct edge plasmons. d) Comparative analysis of EF between flat and trench substrates.

70 nm-thick Au were sequentially deposited on top of the MXene via thermal evaporation with a shadow mask. The channel length and width were 50 and 500 µm, respectively. **Figure** 7a,b illustrate the surface plasmon-assisted device architecture based on the MXene layers. The photocurrent measurement system adopted for photoelectrical evaluation contains power-tunable visible (λ = 532 nm, P = 1437.18 mW cm^{-2}) and NIR (λ = 1064 nm, P = 698.3 mW cm^{-2}) photon sources with a mechanical chopper (1–4000 Hz) to manipulate the laser frequency. The photocurrent was gained by subtracting the dark current from the total current under laser illumination.

Figure 7c–f reveals the time-dependent photocurrent dynamics of the photodetectors based on MXene films on flat Si/SiO$_2$ and Si/SiO$_2$ trench substrates at 15 and 1.5 V bias voltages and chopper frequency of 1 Hz under periodic laser illumination with wavelengths of 532 and 1064 nm. The precipitous and reliable

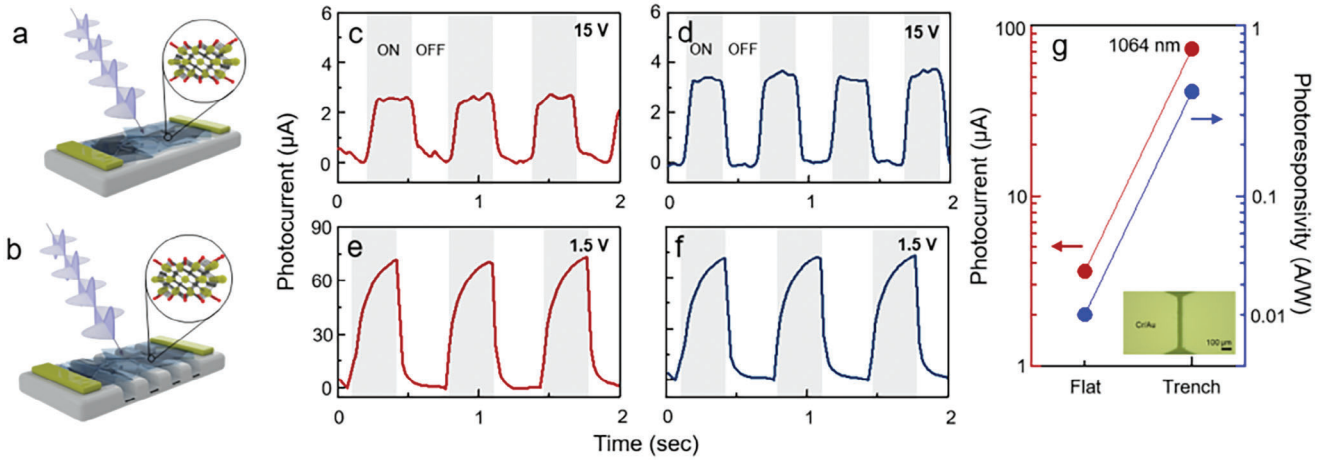

Figure 7. Schematic illustration of the MXene-based photodetectors on a) flat Si/SiO$_2$ and b) Si/SiO$_2$ trench substrates with a line-width 40 nm and a depth of 100 nm. Photoelectrical properties of the MXene-based photodetectors under laser irradiation (532 nm) with c) flat Si/SiO$_2$ and e) Si/SiO$_2$ trench substrates. Photoelectrical properties of the MXene-based photodetectors under laser irradiation (1064 nm) with d) flat Si/SiO$_2$ and f) Si/SiO$_2$ trench substrates. g) Plots of photocurrents and photoresponsivities of the MXene-based photodetectors based on flat Si/SiO$_2$ and Si/SiO$_2$ trench substrates.

photon-stimulated photocurrent switching behavior is distinctly discernible under repeated illumination, irrespective of the sample and laser wavelength, demonstrating excellent reliability and reversibility of the photodetectors. The photocurrents yielded from the photodetectors based on MXene films on Si/SiO_2 trench are assessed to be 73 (532 nm) and 73 μA (1064 nm), respectively, which are 26 and 20 times higher than those of the photodetector based on MXene films on flat Si/SiO_2 (2.8 (532 nm) and 3.6 μA (1064 nm)), as displayed in Figure 7g and Figure S10 (Supporting Information).

Detailed photodetector performance, such as photoresponsivity, detectivity, external quantum efficiency (EQE), and response time were summarized in Table S1 (Supporting Information). The photodetectors based on partially freestanding MXene on Si/SiO_2 trench exhibit evident broad photoresponse in the range of 532 (visible) -1064 nm (NIR), high photoresponsivity (0.2 A W^{-1}@532 nm and 0.41 A W^{-1}@1064 nm), detectivity (2.5×10^7 cm·$Hz^{1/2}$ W^{-1}@532 nm and 5.1×10^7 cm $Hz^{1/2}$ W^{-1}@1064 nm), EQE (47.3%@532 nm and 48.7%@1064 nm), and response time (212@532 nm and 207 μs@1064 nm). The developed photodetector exhibits significantly improved response time and photoresponsivity characteristics, surpassing those of previously reported Ti_3C_2 MXene-based photodetectors. Moreover, it demonstrates superior optical properties, extending into the NIR range, when compared to photodetectors based on other compositions of MXene (Table S2, Supporting Information). In addition, we ascertained the *I–V* characteristics under dark state, verifying in sample-independent ohmic behavior and discernible enhancement of current for partially freestanding MXene on Si/SiO_2 trench (Figure S10, Supporting Information).

The photoresponse of 2D MXene is principally governed by its surface plasmon-assisted energetic hot carriers. The 2D MXene films consisting of the flakes possess a high density of edges and nanometric gaps, which motivates the relaxation of plasmonic momentum constraints for boosting hot electrons generation.[11] Simultaneous enhancement of photoelectrical performance and electrical conductivity for partially freestanding MXene films on Si/SiO_2 trench is indeed attributable to enhanced photoexcited electron transitions. The electrons are stimulated by amplifying surface plasmonic effects of partially freestanding MXene by adopting Si/SiO_2 trench and exclusion of active charge trapping sites.

3. Conclusion

In this study, we aimed to unleash the potential of the plasmonic utilization of 2D MXenes across various optical domains through the incorporation of 3D trench nanostructures produced via the nanofabrication process. Particularly, we endeavored to gain profound insights into the plasmonic light amplification phenomenon occurring at extremely thin thicknesses of MXenes through MXene's interaction with nanostructures. At the sub-monolayer level, MXene generated more hot spots due to the influence of the edge area, which greatly contributed to the plasmonic phenomenon of MXene itself. In addition, the 3D trench structure used as a substrate not only formed a small gap between MXene and the substrate, leading to the formation of more hot spots, but it also induced a larger plasmonic effect due to the light-focusing effect from the structural features. SERS analysis revealed that Raman intensity increased up to ≈60% coverage of MXene, reaching its maximum value, and subsequently decreased with increasing coverage and thickness of MXene. The depth of the SiO_2 layer in the substrate (flat, 50, 80, 100 nm) influenced Raman intensity, showing an increase with greater depth. Under the condition of MXene 50% coverage on a substrate with a depth of 100 nm, the EF value showed an average value of 2.8. Furthermore, MXene-based transducers for the surface plasmon-driven broadband photodetection were realized by utilizing the nanostructured MXene deposited onto dielectric trenches. The extracted photo-responsivities at 532 (visible) and 1064 nm (NIR) of the MXene-based photodetectors corresponded to 0.2 and 0.41 A W^{-1} at 0 V, respectively. The calculated electric field EF of flakes on both flat and trench substrates, based on finite element method calculations, indicates that the trench structure shows a higher surface and edge plasmonic electric field enhancement. We confirm that the observed signal enhancement, both in the sub-monolayer coverage of MXene flakes and in the 3D trench nanostructures, mainly originates from the strong electric field confinement caused by edge plasmons.

4. Experimental Section

Fabrication of 3D Trench Nanostructures: The fabrication of 3D trench nanostructures commenced with the thermal growth of a 100 nm thick silicon dioxide (SiO_2) layer on a silicon wafer. Following this, consecutive deposition steps were carried out, including the application of a 200 nm thick amorphous carbon layer (ACL) and a 20 nm silicon oxynitride (SiON) layer, accomplished using plasma-enhanced chemical vapor deposition (PECVD). Subsequently, a 20 nm thick bottom anti-reflection coating (BARC) layer and a 90 nm thick photoresist (PR) layer were spin-coated onto the substrate. Photolithography techniques were then applied to define a desired 40 nm wide pattern on the PR layer. The subsequent phase involved dry etching processes to selectively remove the exposed BARC, SiON, ACL, and SiO_2 layers. Finally, the remaining ACL layer was eliminated through O_2 plasma treatment. This comprehensive procedure yielded precisely controlled trench nanostructures on the Si wafer substrate, setting the stage for further applications involving $Ti_3C_2T_x$ MXene.

Fabrication of MXene-Based SERS Chips: Ti_3C_2 MXene was synthesized as described previously.[42] The synthesized MXene was prepared by adjusting the concentration, and the coverage and thickness were controlled by spin coating conditions. At this time, spin coating was performed at 3000 rpm for 1 min, and MXene concentration was set to 0.1–3 mg ml^{-1}. It is difficult to obtain a uniform surface due to the agglomeration of MXene during spin coating. Therefore, to increase the bonding strength between the substrate and MXene, after washing with ethanol, acetone, and isopropyl alcohol, plasma cleaning (Air, 100 W, 10 min) was performed, and then a 50:1 mixture of acetone: APTES was used. The surface was treated by stirring at 350 rpm for 1 min. The surface-treated substrate had improved bonding strength with MXene, reduced agglomeration, and increased yield during spin coating. For coating samples of each MXene concentration, 7 μl of R6G was applied per 1 mm^2 and then completely dried at room temperature. Raman was analyzed to evaluate the SERS performance of the prepared sample. At this time, the Raman measurement conditions of layer power, scan time, and points were 4 mW, 500 ms, and 16 points respectively.

Fabrication of Nanostructured MXene-Based Photodetectors: A two-terminal photodetector-based on MXene was fabricated on 300 nm-thick SiO_2/Si with Cr (3 nm)/Au (70 nm) electrodes patterned by thermal evaporation through a shadow mask, in which the channel length and width correspond to 50 and 500 μm, respectively. The SiO_2/Si trench devices with MXene are fabricated using the same process. The photoelectrical properties of the MXene-based photodetector were evaluated in air using

a Keithley 2612B source meter at room temperature. The wavelength of the excitation laser sources were 532 and 1064 nm. A mechanical chopper was utilized to manipulate the laser frequency.

Optical Simulation: Commercial finite element method software (COMSOL Multiphysics) was used to calculate the electric field distribution and electric field EF of the MXene flakes positioned on top of both flat and trench substrates. The dielectric function of MXene was obtained from ellipsometry data of fully covered MXene film. The electric field EF of MXene was obtained by calculating the maximum value within a spatial range from the surface of MXene. The spatial range was set to 1 nm, which is comparable with the molecular size of R6G. To calculate the total EF as a function of coverage, the EF of the surface region and boundary region was weighted by effective surface area (EF x Effective surface area). The boundary area was estimated as the product of boundary length and calculation length (1 nm).

Characterization: UV-vis absorption spectroscopy was employed to characterize the optical properties of the synthesized MXene and R6G. Absorbance measurements were conducted in the wavelength range of 300 to 800 nm. A broadband, indicative of the π-plasmon of MXene, was observed at 750 nm, while the absorption peak of R6G was identified at 527 nm. The structure of the coated MXene was analyzed using SEM (Hitachi). The coverage and thickness of the MXene coating varied with the concentration of the MXene aqueous solution, ranging from 10 to 100%. SEM imaging revealed MXene flakes with an average size of 1.84 ± 0.63 µm.

Supporting Information

Supporting Information is available from the Wiley Online Library or from the author.

Acknowledgements

M.J., S.H.K., and S.K. contributed equally to this work. This work was supported by the National Research Foundation (NRF) of Korea (NRF-2015M3A7B6027973 and NRF-2021M3H4A1A03047333), funded by the Ministry of Science and ICT, Korea. This work was supported by the Semiconductor-Secondary Battery Interfacing Platform Technology Development Project of NNFC and was supported by the Ministry of Trade, Industry and Energy of the Korean Government (RS-2022-00154820). The authors are grateful to Kyoungha Min, Gyu Yeon Lee, and Hyeong Jin Kim for the assistance in the preparation of the MXenes (NNFC). The authors also express their gratitude to prof. Jeong-Hyun Cho (University of Minnesota) for his valuable advice on this work.

Conflict of Interest

The authors declare no conflict of interest.

Data Availability Statement

The data that support the findings of this study are available from the corresponding author upon reasonable request.

Keywords

edge plasmons, MXenes, photodetectors, plasmonics, surface-enhanced Raman scattering

Received: March 27, 2024
Revised: June 17, 2024
Published online:

[1] S. Mehla, A. Kandjani, V. Coyle, C. J. Harrison, M. X. Low, R. B. Kaner, Y. Sabri, S. K. Bhargava, *ACS Appl. Nano Mater* **2022**, *5*, 1873.
[2] J. Langer, D. Jimenez de Aberasturi, J. Aizpurua, R. A. Alvarez-Puebla, B. Auguié, J. J. Baumberg, G. C. Bazan, S. E. J. Bell, A. Boisen, A. G. Brolo, J. Choo, D. Cialla-May, V. Deckert, L. Fabris, K. Faulds, F. J. Garcíade Abajo, R. Goodacre, D. Graham, A. J. Haes, C. L. Haynes, C. Huck, T. Itoh, M. Käll, J. Kneipp, N. A. Kotov, H. Kuang, E. C. L. Ru, H. K. Lee, J.-F. Li, X. Y. Ling, et al., *ACS Nano* **2020**, *14*, 28.
[3] H. L. Wang, E. M. You, R. Panneerselvam, S. Y. Ding, Z. Q. Tian, *Light Sci. Appl.* **2021**, *10*, 161.
[4] K. M. Baek, J. Kim, S. Kim, S. H. Cho, M. S. Jang, J. Oh, Y. S. Jung, *Chem. Mater.* **2018**, *30*, 6183.
[5] T. Wu, Y. W. Lin, *Appl. Surf. Sci.* **2018**, *435*, 1143.
[6] J. M. Kim, C. Lee, Y. Lee, J. Lee, S. J. Park, S. Park, J. M. Nam, *Adv. Mater.* **2021**, *33*, 2006966.
[7] L. Jensen, C. M. Aikens, G. C. Schatz, *Chem. Soc. Rev.* **2008**, *37*, 1061.
[8] X. Song, Y. Wang, F. Zhao, Q. Li, H. Q. Ta, M. H. Rümmeli, C. G. Tully, Z. Li, W. J. Yin, L. Yang, K. B. Lee, J. Yang, I. Bozkurt, S. Liu, W. Zhang, M. Chhowalla, *ACS Nano* **2019**, *13*, 8312.
[9] P. Miao, J. K. Qin, Y. Shen, H. Su, J. Dai, B. Song, Y. Du, M. Sun, W. Zhang, H. L. Wang, C. Y. Xu, P. Xu, *Small* **2018**, *14*, 1704079.
[10] X. Wang, S. C. Huang, S. Hu, S. Yan, B. Ren, *Nat. Rev. Phys.* **2020**, *2*, 253.
[11] D. B. Velusamy, J. K. El-Demellawi, A. M. El-Zohry, A. Giugni, S. Lopatin, M. N. Hedhili, A. E. Mansour, E. Di Fabrizio, O. F. Mohammed, H. N. Alshareef, *Adv. Mater.* **2019**, *31*, 1807658.
[12] J. K. El-Demellawi, S. Lopatin, J. Yin, O. F. Mohammed, H. N. Alshareef, *ACS Nano* **2018**, *12*, 8485.
[13] G. Xie, C. Han, F. Song, Y. Zhu, X. Wang, J. Wang, Z. Wu, X. Xie, N. Zhang, *Nanoscale* **2022**, *14*, 18010.
[14] M. Mojtabavi, A. VahidMohammadi, K. Ganeshan, D. Hejazi, S. Shahbazmohamadi, S. Kar, A. C. T. van Duin, M. Wanunu, *ACS Nano* **2021**, *15*, 625.
[15] Y. I. Jhon, J. Koo, B. Anasori, M. Seo, J. H. Lee, Y. Gogotsi, Y. M. Jhon, *Adv. Mater.* **2017**, *29*, 1702496.
[16] Y. Chen, Y. Ge, W. Huang, Z. Li, L. Wu, H. Zhang, X. Li, *ACS Appl. Nano Mater* **2020**, *3*, 303.
[17] V. Pacheco-Peña, T. Hallam, N. Healy, *Light Sci. Appl.* **2022**, *11*, 22.
[18] A. Sarycheva, T. Makaryan, K. Maleski, E. Satheeshkumar, A. Melikyan, H. Minassian, M. Yoshimura, Y. Gogotsi, *J. Phys. Chem. C* **2017**, *121*, 19983.
[19] A. D. Dillon, M. J. Ghidiu, A. L. Krick, J. Griggs, S. J. May, Y. Gogotsi, M. W. Barsoum, A. T. Fafarman, *Adv. Funct. Mater.* **2016**, *26*, 4162.
[20] C. Lin, Y. Li, Y. Peng, S. Zhao, M. Xu, L. Zhang, Z. Huang, J. Shi, Y. Yang, *J. Nanobiotechnol.* **2023**, *21*, 149.
[21] H. Xie, P. Li, J. Shao, H. Huang, Y. Chen, Z. Jiang, P. K. Chu, X.-F. Yu, *ACS Sens.* **2019**, *4*, 2303.
[22] N. T. T. Phuong, L. H. Tho, T. T. Nguyen, N. N. Nam, K. T. L. Trinh, *Sens. Actuat., A* **2023**, *363*, 114714.
[23] W. Zhu, R. Esteban, A. G. Borisov, J. J. Baumberg, P. Nordlander, H. J. Lezec, J. Aizpurua, K. B. Crozier, *Nat. Commun.* **2016**, *7*, 11495.
[24] J.-M. Nam, J.-W. Oh, H. Lee, Y. D. Suh, *Acc. Chem. Res.* **2016**, *49*, 2746.
[25] T. B. Limbu, B. Chitara, M. Y. Garcia Cervantes, Y. Zhou, S. Huang, Y. Tang, F. Yan, *J. Phys. Chem. C* **2020**, *124*, 17772.
[26] L.-Å. Näslund, P. O. Å. Persson, J. Rosen, *J. Phys. Chem. C* **2020**, *124*, 27732.
[27] A. C. Y. Yuen, T. B. Y. Chen, B. Lin, W. Yang, I. I. Kabir, I. M. D. C. Cordeiro, A. E. Whitten, J. Mata, B. Yu, H.-D. Lu, G. H. Yeoh, *Compos. Part C: Open Access* **2021**, *5*, 100155.
[28] A. Sarycheva, Y. Gogotsi, *Chem. Mater.* **2020**, *32*, 3480.

[29] F. Zhang, R. Cao, Z. Li, S. Gao, H. Chen, J. Guo, Y. Zhang, B. O. Al-Amoudi, S. Wageh, A. A. Al-Ghamdi, X. Zhang, H. Zhang, *Nanophotonics* **2022**, *11*, 3139.
[30] F. Salehtash, A. Annušová, A. Stepura, Y. Soyka, Y. Halahovets, M. Hofbauerová, M. Mičušík, M. Kotlár, P. Nádaždy, P. Albrycht, P. Šiffalovič, M. Jergel, M. Omastová, E. Majková, *Materials* **2024**, *17*, 1385.
[31] S. Elumalai, J. R. Lombardi, M. Yoshimura, *Mater. Adv.* **2020**, *1*, 146.
[32] R. Kang, Z. Zhang, L. Guo, J. Cui, Y. Chen, X. Hou, B. Wang, C.-T. Lin, N. Jiang, J. Yu, *Sci. Rep.* **2019**, *9*, 9135.
[33] M. Mustakeem, J. K. El-Demellawi, M. Obaid, F. Ming, H. N. Alshareef, N. Ghaffour, *ACS Appl. Mater. Interfaces* **2022**, *14*, 5265.
[34] M. Jang, D. Jung, J. Kim, J. Cho, S. Yim, W. Song, S. Myung, S. S. Lee, K.-S. An, *J. Alloys Compd.* **2023**, *947*, 169563.
[35] K. Chaudhuri, M. Alhabeb, Z. Wang, V. M. Shalaev, Y. Gogotsi, A. Boltasseva, *ACS Photonics* **2018**, *5*, 1115.
[36] C. Park, N.-R. Park, J. Kwon, H. Kim, Y. Gogotsi, C. M. Koo, M.-K. Kim, *Adv. Mater.* **2024**, *36*, 2309189.
[37] P. Machata, M. Hofbauerová, Y. Soyka, A. Stepura, D. Truchan, Y. Halahovets, M. Mičušík, P. Šiffalovič, E. Majková, M. Omastová, *J. Colloid Interface Sci.* **2022**, *622*, 759.
[38] D. Rodrigo, O. Limaj, D. Janner, D. Etezadi, F. J. García de Abajo, V. Pruneri, H. Altug, *Science* **2015**, *349*, 165.
[39] A. N. Grigorenko, M. Polini, K. S. Novoselov, *Nat. Photonics* **2012**, *6*, 749.
[40] M. Abutoama, I. Abdulhalim, *Opt. Express* **2015**, *23*, 28667.
[41] Y. D. Kim, H. Kim, Y. Cho, J. H. Ryoo, C.-H. Park, P. Kim, Y. S. Kim, S. Lee, Y. Li, S.-N. Park, Y. S. Yoo, D. Yoon, V. E. Dorgan, E. Pop, T. F. Heinz, J. Hone, S.-H. Chun, H. Cheong, S. W. Lee, M.-H. Bae, Y. D. Park, *Nat. Nanotechnol.* **2015**, *10*, 676.
[42] S. Y. Jeong, Y. Jeon, E. Kim, G. Lee, Y.-W. Oh, C. W. Ahn, E. H. Cho, Y. Lee, K. C. Choi, *ACS Nano* **2023**, *17*, 10353.